THE JOURNAL OF PHYSICAL CHEMISTRY A

Article

Cite This: J. Phys. Chem. A 2018, 122, 3480−3488

pubs.acs.org/JPCA

Predicting Intersystem Crossing Rates with AIMS-DFT Molecular Dynamics

Dmitry A. Fedorov,[†,§] Aleksandr O. Lykhin,[†,‡] and Sergey A. Varganov*[,†]

[†]Department of Chemistry, University of Nevada, Reno, 1664 North Virginia Street, Reno, Nevada 89557-0216, United States

[‡]Department of Chemistry, Siberian Federal University, 79 Svobodny Prospect, Krasnoyarsk, Krasnoyarsk krai, 660041, Russia

Supporting Information

ABSTRACT: Accurate prediction of the intersystem crossing rates is important for many different applications in chemistry, physics, and biology. Recently, we implemented the ab initio multiple spawning (AIMS) molecular dynamics method to describe the intersystem crossing processes, where nonradiative transitions between electronic states with different spin multiplicities are mediated by spin−orbit coupling. Our original implementation of the direct AIMS dynamics used the complete active space self-consistent field (CASSCF) method to describe multiple coupled electronic states on which multidimensional Gaussian wave packets were propagated. In this work, we improve the computational efficiency and versatility of the AIMS dynamics by interfacing it with the density functional theory (DFT). The new AIMS-DFT and the earlier AIMS-CASSCF implementations are used to investigate the effects of electronic structure methods on the predicted intersystem crossing rate constants and the lowest triplet state lifetime in the GeH_2 molecule. We also compare the rates and lifetimes obtained from the AIMS simulations with those predicted by the statistical nonadiabatic transition state theory (NA-TST). In NA-TST, the probabilities of spin transitions are calculated using the Landau−Zener, weak coupling, and Zhu−Nakamura formulas. Convergence of the AIMS rate constants with respect to the simulation time and the number of initial trajectories (Gaussian wave packets) is analyzed. An excellent agreement between AIMS-DFT and AIMS-CASSCF can be explained by cancelation of two effects: higher energy barriers and a stronger spin−orbit coupling in DFT relative to CASSCF. The rate constants obtained with the AIMS-DFT dynamics are about a factor of 2 larger than those predicted by the statistical NA-TST. This is likely due to the importance of the nonlocal interstate transitions missing from the NA-TST description.

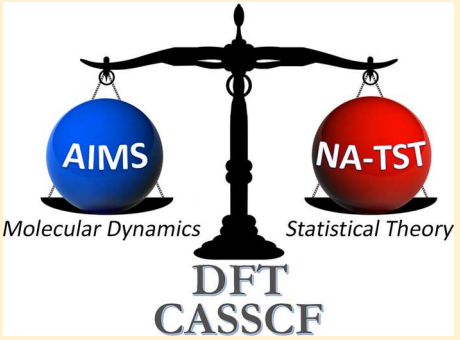

I. INTRODUCTION

Intersystem crossings (ISC), nonradiative transitions between the electronic states of different spin multiplicities mediated by spin−orbit coupling (SOC), are important in a variety of different systems. Because SOC is stronger in molecules that contain heavy elements, many metal complexes are characterized by relatively fast ISCs between electronic states. For example, ISCs play a crucial role in the deactivation process in organometallic complexes proposed for the use in OLEDs,[1] dye-sensitized solar cells,[2] and other devices.[3] In metal−sulfur proteins, such as [NiFe]-hydrogenase[4] and rubredoxin,[5] nonradiative transitions between the electronic states of the active sites could play important roles in catalytic activity and electron transfer. Even in organic molecules without heavy elements, where SOC is much weaker, ISCs can compete with other types of excited state relaxation.[6−11] Hence ISCs, along with internal conversions and radiative processes, are central to the photochemistry and photophysics of many different molecular systems.[12−19]

The ISC rates can be calculated using two different approaches. The time-independent approach uses statistical mechanics and requires the knowledge of molecular properties at few critical points on the potential energy surfaces (PESs) of the relevant electronic states. The time-dependent approach is based on the propagation of the classical or semiclassical nuclei on PESs, as in molecular dynamics. One of the statistical approaches is the nonadiabatic transition state theory (NA-TST),[20,21] an extension of the conventional single-state transition state theory to reactions that involve multiple electronic states. In NA-TST, the ISC rate constants are calculated from the molecular properties at the two critical points on PESs: a minimum corresponding to reactants and a minimum energy crossing point (MECP), which is the lowest energy point on the crossing seam of two spin-diabatic PESs. To carry out the NA-TST rate calculations, the density of rovibrational states at the reactants and MECP, as well as interstate transition probability, must be known. The density of states can be obtained using the rigid rotor and harmonic oscillator models; however, more sophisticated methods can be used. The probability of the SOC-mediated transition can be calculated using the simple Landau−Zener (LZ) formula,[22−24] the weak coupling (WC) formula[25,26] that accounts for

Received: January 25, 2018
Revised: March 12, 2018
Published: March 13, 2018

DOI: 10.1021/acs.jpca.8b00883
J. Phys. Chem. A 2018, 122, 3480−3488

quantum tunneling and interference between reaction paths, or the more complex Zhu−Nakamura (ZN) formulas.[27]

In the time-dependent approach, there are no assumptions about the importance of any particular PES geometries, and the ISC rates are obtained by averaging different reaction pathways through nonadiabatic molecular dynamics simulations. Thus, in addition to solving the time-independent Schrödinger equation for electrons, the time-dependent Schrödinger equation (TDSE) for nuclei has to be solved. In quantum dynamics, the nuclei are treated as quantum wave packets. In general, this requires the knowledge of full PESs due to the nonlocal nature of quantum wave packets. Therefore, applications of quantum dynamics are limited to small systems, for which the multidimensional PESs can be constructed. To avoid the construction of full PESs, in ab initio molecular dynamics (AIMD), the electronic structure calculations are done "on-the-fly" as nuclei propagate along the classical or semiclassical trajectories. The most common type of nonadiabatic AIMD is the trajectory surface hopping (TSH) method, in which a swarm of classical trajectories represents a nuclear wave packet. Each trajectory is propagated on a PES of the specific electronic state. Switches (hops) between electronic states occur in a stochastic manner with a probability dependent on the state populations and SOC between the states.

In contrast to TSH, in the ab initio multiple spawning (AIMS) method,[28] the nuclear wave packets are represented by the frozen multidimensional Gaussian nuclear basis functions (NBFs). This representation ensures the locality of the wave function, and therefore still allows the use of the "on-the-fly" AIMD approach. The AIMS dynamics accounts for quantum effects in a natural way: the expansion coefficients (amplitudes) of the nuclear wave function in the basis of NBFs are propagated by solving the TDSE. The positions and momenta of NBFs are propagated using the classical equations of motion. The nuclear basis set is expanded in a physically meaningful way by adding (spawning) new NBFs in the regions of strong interstate coupling. If no approximations are used, the AIMS method converges to the exact solution of TDSE as the number of NBFs increases. The AIMS method to study ISCs has been interfaced with the GAMESS[29] and MOLPRO[30] electronic structure packages.

In our previous work, we extended the AIMS method, originally developed to describe internal conversion processes, to ISC dynamics using the multireference CASSCF method for electronic structure calculations.[29] Multireference methods can describe ground and excited electronic states at different molecular geometries, including bond breaking and dissociation, in a qualitatively correct manner. However, choosing the CASSCF active space to describe all the geometries accessible in an AIMD simulation could be a very challenging task. Also, the CASSCF method does not account for most of the dynamic correlation between electrons, which could result in very inaccurate electronic state energies, and hence in flawed nonadiabatic AIMD simulations. In this work, we explore the possibility of using a robust and computationally efficient DFT method to perform the AIMS dynamics simulations. Although DFT is a single-reference method, which can have difficulties describing the bond breaking and dissociation processes, it has three major advantages over the CASSCF method: (1) it recovers a significant part of the dynamic correlation energy; (2) it is less computationally expensive, and therefore can be applied to larger systems and slower ISCs when used for the AIMS dynamics simulations; (3) it is a "black box" method that eliminates the need for constructing the CASSCF active spaces. Here, we apply our new AIMS-DFT implementation to the ISC kinetics and dynamics involving nonadiabatic transitions between the lowest singlet $^1A_1$ and triplet $^3B_1$ states of GeH_2. We compare the AIMS-DFT and AIMS-CASSCF dynamics[29] results and analyze how different electronic structure methods affect the predicted ISC rates and excited state lifetime. In addition, we compare the AIMS molecular dynamics results with those obtained from the statistical NA-TST calculations where transition probabilities between electronic states are computed using the ZN, LZ, and WC formulas.

The paper is organized as follows. In section II, the NA-TST and the AIMS nonadiabatic dynamics are briefly described. In section III, the details of the NA-TST and AIMS calculations are provided. Section IV reports and discusses the ISC rate constants and the excited state lifetime obtained using different statistical and molecular dynamics methods. The summary and concluding remarks are presented in Section V.

II. THEORETICAL METHODS

A. Nonadiabatic Transition State Theory. The detailed discussion of NA-TST can be found in our recent review.[31] The NA-TST rate constant as a function of internal energy E is[20,21,31,32]

$$k(E) = \frac{1}{h\rho_R(E)} \int_0^E \rho_{\mathrm{MECP}}(E - \varepsilon_\perp) P_{\mathrm{trans}}(\varepsilon_\perp) d\varepsilon_\perp \tag{1}$$

where h is the Planck constant, $\varepsilon_\perp$ is the reaction coordinate energy orthogonal to the crossing seam between two spin-diabatic PESs, $\rho_R(E)$ and $\rho_{\mathrm{MECP}}(E - \varepsilon_\perp)$ are the densities of rovibrational states of reactants and at MECP, and $P_{\mathrm{trans}}(\varepsilon_\perp)$ is the probability of transition between the PESs. It is important to point out that in the case of ISC, there is only one coordinate orthogonal to the crossing seam between two PESs with different spin multiplicities. This is contrary to the case of internal conversion through a conical intersection, where two such coordinates are present.[31]

The LZ formula,[26,33] expresses the double passage transition probability as

$$P_{\mathrm{trans}}(\varepsilon_\perp) = 1 - P_{\mathrm{LZ}}^2 \tag{2}$$

$$P_{\mathrm{LZ}} = \exp\left(\frac{-2\pi H_{\mathrm{SOC}}^2}{\hbar |\Delta \mathbf{G}|} \sqrt{\frac{\mu_\perp}{2(\varepsilon_\perp - E_{\mathrm{MECP}})}} \right) \tag{3}$$

In eq 3, H_{SOC} and $\Delta\mathbf{G} = \mathbf{G_1} - \mathbf{G_2}$ are the SOC and the difference of the gradients of two PESs at the MECP, respectively; $\mu_\perp$ is the reduced mass of the degree of freedom orthogonal to the crossing seam; E_{MECP} is the energy of MECP with respect to the reactants. In contrast to the LZ formula, the following WC formula accounts for quantum tunneling and interference between reaction pathways.[25,26,34]

$$P_{\mathrm{trans}}(\varepsilon_\perp) = 4\pi^2 H_{\mathrm{SOC}}^2 \left(\frac{2\mu_\perp}{\hbar^2 \bar{G} |\Delta \mathbf{G}|} \right)^{2/3} \times \mathrm{Ai}^2 \left[-(\varepsilon_\perp - E_{\mathrm{MECP}}) \left(\frac{2\mu_\perp |\Delta \mathbf{G}|^2}{\hbar^2 \bar{G}^4} \right)^{1/3} \right] \tag{4}$$

Here $\bar{G} = |\mathbf{G_1}\mathbf{G_2}|^{1/2}$ is the geometric mean of the PES gradients at the MECP, and Ai is the Airy function. On the other hand, the ZN formulas[35−37] provide more rigorous estimates for the

DOI: 10.1021/acs.jpca.8b00883
J. Phys. Chem. A 2018, 122, 3480−3488

transition probabilities by taking into account both tunneling and nonlinear behavior of the potential energy curves along the reaction path. The double passage ZN probability for a sloped intersection can be written as

$$P_{\text{trans}}(\varepsilon_\perp) = 4P_{\text{ZN}}(1 - P_{\text{ZN}})\sin^2(\psi) \tag{5}$$

where P_{ZN} and ψ define a single passage probability and a total phase, respectively. In contrast to the WC formula, the ZN formulas cover all strength of spin−orbit coupling with P_{ZN} given by

$$P_{\text{ZN}} = \begin{cases} \exp\left[-\frac{\pi}{4a}\sqrt{\frac{2}{b^2 + \sqrt{b^4 + 0.4a^2 + 0.7}}}\right], & b(\varepsilon_\perp) \geq 0 \\ [1 + B(\sigma/\pi)\exp(2\delta) - g_2\sin^2(\sigma)]^{-1}, & b(\varepsilon_\perp) < 0 \end{cases} \tag{6}$$

$$B(x) = \frac{2\pi x^{2x}\exp(-2x)}{x\Gamma^2(x)} \tag{7}$$

$$g_2 = \frac{3\sigma}{\pi\delta}\ln(1.2 + a^2) - \frac{1}{a^2} \tag{8}$$

The spin-adiabatic parameters a and $b(\varepsilon_\perp)$ together with the phases σ, δ, and ψ are given in SI (eqs S3−S27). To obtain harmonic frequencies at the MECP for degrees of freedom parallel to the crossing seam, first, an effective Hessian is constructed.[31] Then the projection operator is applied to remove the translational, rotational, and reaction degrees of freedom. Finally, the effective Hessian is diagonalized to obtain the 3N-7 harmonic frequencies of the crossing seam. These frequencies are used to calculate the density of vibrational states at the MECP. The rovibrational densities of states at the MECP and at the reactants are calculated as convolutions of the harmonic vibrational states density[38] with the rotational states densities.[39]

B. Ab Initio Multiple Spawning for ISC Dynamics. The detailed review of the AIMS method to describe internal conversion dynamics can be found elsewhere.[28,40−42] Our implementation to study the ISC dynamics is described in the previous work.[29] Briefly, the total wave function is a linear combination of the products of electronic and nuclear wave functions:

$$\psi = \sum_I \sum_k^{N_I(t)} C_k^I(t)\chi_k^I(R; \bar{R}_k^I(t), \bar{P}_k^I(t), \bar{\gamma}_k^I(t), \alpha_{\rho_k})\phi_I(r; R) \tag{9}$$

In eq 9, ϕ_I is the wave function of the electronic state I. The nuclear wave function is a superposition of the frozen Gaussian NBFs χ_k^I with time-dependent complex amplitudes C_k^I; k labels NBFs, and $N_I(t)$ is the number of NBFs on the electronic state I. The NBFs χ_k^I are parametrized with the time-independent width α_{ρ_k} and the time-dependent average position $\bar{R}_k^I(t)$, momentum $\bar{P}_k^I(t)$ and phase $\bar{\gamma}_k^I(t)$. The positions and momenta are propagated according to the classical Hamilton equations; the phase is propagated semiclassically. The time-independent Gaussian width, α_{ρ_k}, depends only on the type of the nucleus and does not depend on either the NBF (trajectory) index k or the electronic state index I.[43]

The following TDSE written in matrix form is solved for the complex amplitudes C_k^I,

$$\frac{d\mathbf{C}^I}{dt} = -i\mathbf{S}_{II}^{-1}\left\{[\mathbf{H}_{II} - i\dot{\mathbf{S}}_{II}]\mathbf{C}^I + \sum_{J\neq I}\mathbf{H}_{IJ}\mathbf{C}^J\right\} \tag{10}$$

The overlap of the NBFs and its time derivative are expressed as

$$(S_{II})_{kl} = \langle\chi_k^I|\chi_l^I\rangle \tag{11}$$

$$(\dot{S}_{II})_{kl} = \langle\chi_k^I|\frac{\partial}{\partial t}|\chi_l^I\rangle \tag{12}$$

The diagonal matrix element, $\mathbf{H}_{II}$, is the sum of the kinetic and potential energies of the electronic state I. The off-diagonal elements are the effective SOC matrix elements:

$$(H_{IJ})_{kl} = \langle\chi_k^I\phi_I|\hat{H}_e|\phi_J\chi_l^J\rangle = \langle\chi_k^I|\langle\phi_I|\hat{H}_{\text{SO}}|\phi_J\rangle|\chi_l^J\rangle \tag{13}$$

Eq 13 can be simplified by using the first-order saddle-point approximation,[44]

$$\langle\chi_k^I|\langle\phi_I|\hat{H}_{\text{SO}}|\phi_J\rangle|\chi_l^J\rangle \approx \langle\phi_I|\hat{H}_{\text{SO}}(R_C)|\phi_J\rangle\langle\chi_k^I|\chi_l^J\rangle \tag{14}$$

where R_C is the centroid position of the product of the Gaussian NBFs χ_k^I and χ_l^J.

We treat the electronic state components with different magnetic quantum numbers M_s arising from the same state with spin S as a single spin-diabatic state. This approximation could lead to the loss or rotation invariance;[31,45] however, the effect is expected to be insignificant for the system with relatively weak SOC considered here. To calculate the electronic SOC matrix elements, we use the Breit−Pauli spin−orbit operator with one- and two-electron terms.[46] The effective SOC is calculated as a root-mean-square over the magnetic quantum numbers M_s and M_s',

$$H_{\text{SOC}} = \langle\phi_I|\hat{H}_{\text{SO}}|\phi_J\rangle = \sqrt{\sum_{M_S=-S}^{S}\sum_{M_S'=-S'}^{S'}|\langle SM_S|\hat{H}_{\text{SO}}|S'M_S'\rangle|^2} \tag{15}$$

If during the propagation of NBF χ_k^I on electronic state I the SOC between states I and J becomes large, then a NBF χ_l^J on the state J could be added (spawned). The spawning occurs only if the dimensionless effective coupling parameter

$$\Lambda_{\text{eff}} = \frac{\langle\phi_I|\hat{H}_{\text{SO}}(R_C)|\phi_J\rangle\langle\chi_k^I|\chi_l^J\rangle}{E_I - E_J} \tag{16}$$

is larger than a predefined threshold.[47] In eq 16, E_I and E_J are the potential energies of the electronic states I and J. New NBFs are created with no initial population. The population transfer between states occurs during the propagation of the NBF amplitudes C_k^I (eq 10).

Population transfer between singlet and triplet electronic states is described by the following kinetics equation:

$$F_3 \underset{k_1}{\overset{k_3}{\rightleftarrows}} F_1 \tag{17}$$

where F_3 and F_1 are the populations of the triplet and singlet states; k_3 and k_1 are the ISC rate constants. Assuming that initially only triplet state is populated ($F_3(t_0) = 1$), the solution of the rate eq 17 is[48]

$$F_3(t) = (F_3(t_0) - k_1\tau)\exp\left(-\frac{t - t_0}{\tau}\right) + k_1\tau \tag{18}$$

DOI: 10.1021/acs.jpca.8b00883
J. Phys. Chem. A 2018, 122, 3480−3488

where $\tau = 1/(k_1 + k_3)$ is the triplet state lifetime. The population of state I is a sum of the populations from each NBF propagated on this state (F_k^I).

$$F_I = \sum_{k=1}^{N_I} F_k^I \tag{19}$$

The rate constants k_1, k_3 are obtained by least-squares fitting the triplet state population F_3 with eq 18.

III. COMPUTATIONAL DETAILS

In our implementation, the AIMS code propagates NBFs and their complex amplitudes, while the GAMESS suite of programs calculates the electronic state energies, energy gradients, molecular orbitals and SOC.[29] In this work, the GAMESS calculations on GeH_2 were performed using the state-specific complete active space self-consistent field (CASSCF)[49] and unrestricted DFT (B3LYP)[50−52] methods with the 6-31G* basis set. In the CASSCF calculations, the full valence active space with 6 electrons on 6 orbitals was used. SOC was computed with the CAS-CI, and the partial 2-electron method (HSO2P).[53] In the AIMS-CASSCF dynamics, the orbitals for CAS-CI were obtained from the state-averaged CASSCF calculations. Because currently GAMESS is not capable of calculating SOC with the DFT methods, in the AIMS-DFT dynamics, SOC was obtained with the CAS-CI method using the high-spin α-set of DFT orbitals. The CAS-CI active space was the same as in the CASSCF calculations.

The lowest energy singlet $^1A_1$ and triplet $^3B_1$ electronic states of GeH_2 were included in the AIMS molecular dynamics simulations. No spatial symmetry restrictions were imposed during the simulations. To avoid any numerical problems with Verlet integration of the classical equations of motion, small time steps (0.1 fs in the region of strong coupling and 0.2 fs everywhere else) were used. The choice of the effective coupling parameter threshold (0.2) was dictated by convergence of the $^3B_1$ population decay with respect to this threshold (Figure S1). It is important to note that a smaller threshold of 0.1 was used in our previous work,[29] therefore, the CASSCF rates and lifetimes reported in two studies are slightly different. For spawning to occur, in addition to $\Lambda_{eff} < 0.2$, the overlap between the parent and the child NBFs must be larger than 0.5. The widths of the Gaussian NBFs were 30 $bohr^{-2}$ and 4.7 $bohr^{-2}$ for the Ge and H atoms, respectively.[43] Each AIMS simulation was initialized with a single NBF on the excited $^3B_1$ state. The initial conditions for the NBF position and momentum were obtained from the Wigner distribution[54,55] generated using the zero-point energy (ZPE) of the ground state equally distributed between the kinetic and potential energy.

IV. RESULTS AND DISCUSSION

The GeH_2 geometries, relative energies, vibrational frequencies, and SOC for the lowest energy singlet ($^1A_1$) and triplet ($^3B_1$) states, as well as for the MECP, calculated with the CASSCF(6,6)/6-31G* and UB3LYP/6-31G* levels of theory are reported in Table 1. The bond lengths and angles calculated with CASSCF and DFT agree well. The harmonic frequencies predicted by DFT are slightly higher than the ones calculated with CASSCF. The SOC values computed using the high-spin α DFT orbitals are somewhat higher than those obtained using the CASSCF state-averaged orbitals. The higher SOC values are expected to increase the ISC rate constants. The energy

Table 1. Bond Length (r), Angle (θ), Energy Relative to the Singlet Minimum (ΔE), Harmonic Vibrational Frequencies (ω), Zero-Point Vibrational Energy (ZPE), and SOC Constant for the $^1A_1$ Minimum, $^3B_1$ Minimum, and MECP Geometries Calculated Using the CASSCF(6,6)/6-31G* and UB3LYP/6-31G* Levels of Theory

	$^1A_1$		$^3B_1$		MECP	
	CASSCF	DFT	CASSCF	DFT	CASSCF	DFT
r, Å	1.621	1.609	1.564	1.559	1.541	1.531
θ, deg	92.4	90.2	118.7	119.0	132.8	136.2
ΔE, cm^{-1}	0	0	7484	9367	8201	10418
ω, cm^{-1}	924	941	806	811	1795	1845
	1839	1880	1991	1966	2151	2177
	1844	1896	2052	2063		
ZPE, cm^{-1}	2304	2359	2425	2420	1973	2011
SOC, cm^{-1}	374	406	367	405	352	389

difference between the minima of $^1A_1$ and $^3B_1$ states predicted by DFT calculations is higher by almost 2000 cm^{-1} compared to CASSCF. The $^1A_1$ to MECP energy barrier obtained with DFT is by 2217 cm^{-1} higher than the CASSCF barrier. More importantly, the $^3B_1$ to MECP barrier predicted by DFT (1051 cm^{-1}) is significantly higher than the same CASSCF barrier (717 cm^{-1}). The higher DFT barrier is expected to result in a smaller $^3B_1 \rightarrow {}^1A_1$ ISC rate constant and a longer lifetime of the $^3B_1$ excited state.

Figure 1 depicts how the geometry of GeH_2 changes with time in one of the AIMS simulations. For clarity, only the first four basis functions are presented, resulting from three spawning events. One could expect that the spawning events would look like bifurcation points where the child basis function is added at the point of maximum coupling and the geometries of the two basis functions match. However, in the AIMS method when a new basis function is added at the point of maximum coupling, this function is propagated back in time to the point where the spawning is initiated (coupling between two states becomes larger than the effective coupling parameter Λ_{eff}). This back-propagation is essential to capture the population transfer not only after the coupling reached its maximum, but before that moment as well. This is the reason why the child basis functions in Figure 1 appear before the point of matching geometries. The details of spawning procedure can be found elsewhere.[28] For all four basis functions, the amplitude of r_2 variation is larger compared to r_1 reflecting the nonequilibrium energy distribution between these degrees of freedom. This distribution depends on the initial conditions (positions and momenta) and is different for each AIMS simulation (initial trajectory). In addition, the distribution can be different for NBFs within one AIMS simulation. For instance, NBF1, NBF2, and NBF3 have similar angle amplitude variations, whereas for NBF4, there is less energy in the bending degree of freedom and more energy in the r_1 stretch.

To allow the direct comparison of the AIMS-DFT and AIMS-CASSCF results, the same number of initial NBFs (trajectories) and simulation time were used. A total number of 48 AIMS simulations were run for 150 fs, each starting with a single NBF on the excited $^3B_1$ state. At time t = 150 fs, each simulation contained on average 25 NBFs resulting in about 1200 total NBFs spawned from the 48 initial NBFs. The population of the $^3B_1$ excited state as a function of time is plotted in Figure 2. The average population of the $^3B_1$ state at

DOI: 10.1021/acs.jpca.8b00883
J. Phys. Chem. A 2018, 122, 3480−3488

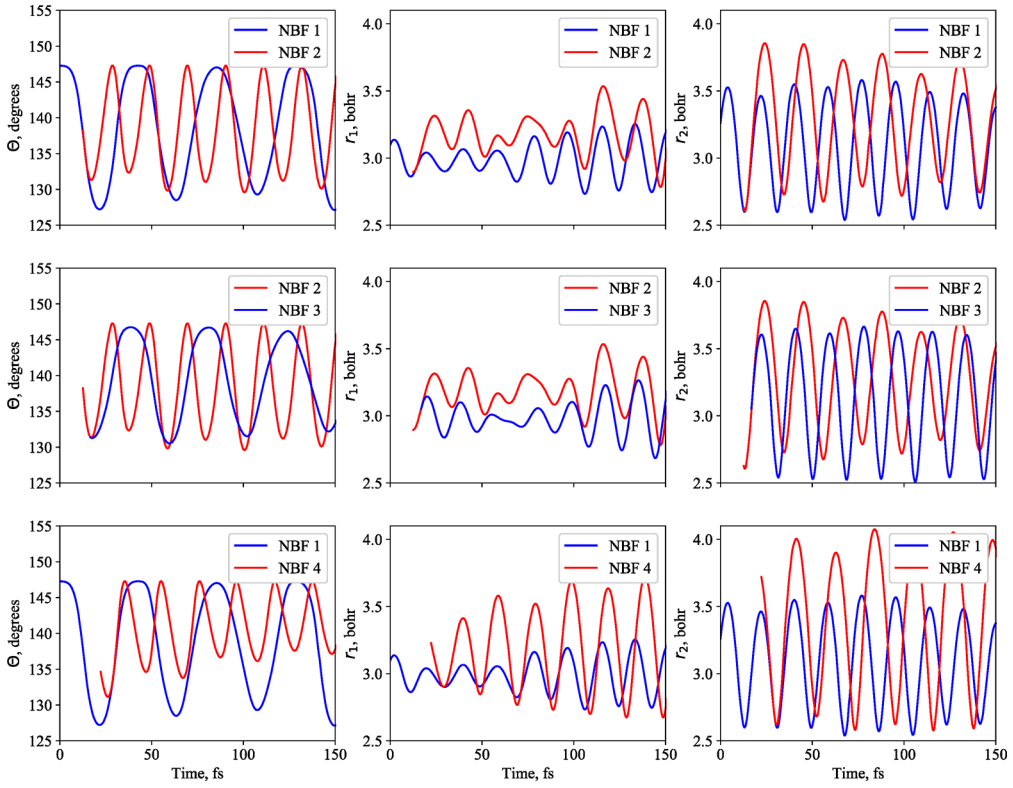

Figure 1. Dependence of the GeH_2 geometry on time in one of the AIMS simulations. First, second, and third columns show angle θ, and the Ge−H distances r_1 and r_2, respectively. Blue lines represent NBFs on the excited $^3B_1$ state, red lines correspond to NBFs on the ground $^1A_1$ state. The first row depicts the spawning of NBF1 propagating on $^3B_1$ state to produce NBF2 on $^1A_1$ state. In the second row, NBF2 spawns NBF3 back to the $^3B_1$ state. The third row shows another spawn of NBF1 on $^3B_1$ to produce NBF4 on $^1A_1$ state.

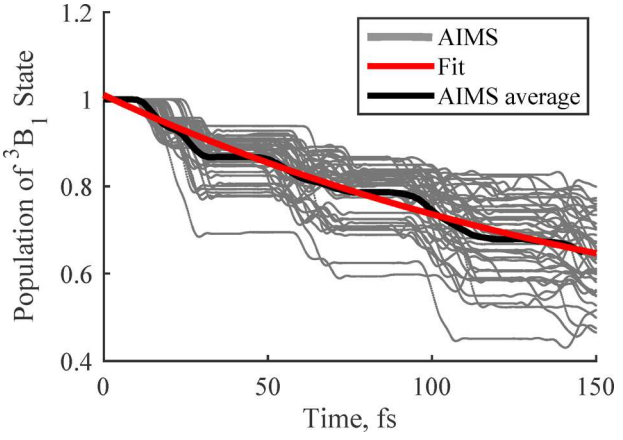

Figure 2. Population of the $^3B_1$ state as a function of time calculated from all 48 simulations using UB3LYP/6-31G*. Gray lines represent the populations from individual simulations; black line is the average population. The first-order decay fit using eq 18 is shown with the red line. The rate constants obtained from the fit are $k_3 = 3.50 \times 10^{12}$ s^{-1} for the $^3B_1 \rightarrow {}^1A_1$ transitions, and $k_1 = 1.99 \times 10^{12}$ s^{-1} for the reverse $^1A_1 \rightarrow {}^3B_1$ transitions. The corresponding $^3B_1$ state lifetime is 182 fs.

each given time was calculated by averaging the populations from all 48 simulations; the values were grouped into 2 fs bins, and a mean value was obtained for each bin. After 150 fs, approximately 40% of the population was transferred from the excited state in the AIMS-DFT simulations, compared to 45% in AIMS-CASSCF. Therefore, the population transfer rate predicted by AIMS-DFT is slightly slower than in AIMS-CASSCF, resulting in the slightly lower rate constants and longer excited state lifetime. For AIMS-DFT, a first-order decay fit with eq 18 predicts the rate constants $k_3 = 3.50 \times 10^{12}$ s^{-1} (3.42×10^{12} s^{-1}, 3.58×10^{12} s^{-1}) for the $^3B_1 \rightarrow {}^1A_1$ transitions, and $k_1 = 1.99 \times 10^{12}$ s^{-1} (1.69×10^{12} s^{-1}, 2.29×10^{12} s^{-1}) for the reverse $^1A_1 \rightarrow {}^3B_1$ transitions. The lifetime of the $^3B_1$ state, τ, is 182 fs (170 fs, 197 fs). The 95% confidence intervals are reported in parentheses; the R^2 value for the fit is 0.696. The corresponding AIMS-CASSCF values are $k_3 = 3.78 \times 10^{12}$ s^{-1} (3.86×10^{12} s^{-1}, 3.71×10^{12} s^{-1}), $k_1 = 1.58 \times 10^{12}$ s^{-1} (1.32×10^{12} s^{-1}, 1.85×10^{12} s^{-1}), and $\tau = 186$ fs (175 fs, 199 fs); the R^2 value is 0.725.

The plot showing the convergence of the AIMS-DFT fitted rate constants for the forward and backward reactions with respect to the total simulation time is presented in Figure 3a. For the simulation time less than 120 fs, the fitting gives the unphysical results predicting k_1 to be larger than k_3. After 120 fs, k_1 starts to converge, and between 145 and 150 fs, it does not change significantly. With respect to the number of initial trajectories (Figure 3b), the fitting provides poor results for less than 30 initial NBFs (trajectories). The k_1 constant oscillates and sometimes even becomes negative. Only for more than 30 initial trajectories is the convergence observed. From the analysis of Figure 3, we can conclude that the forward rate constant k_3 is predicted with significantly higher accuracy than the reverse constant k_1. To predict k_1 accurately, a larger number of longer trajectories is needed. It is important to point out that the goodness-of-fit data only provides information about the fitting procedure itself, and does not give an insight into the error coming from the insufficient sampling (number and length of trajectories). For instance, in Figure 3a, the k_1 constant changes almost by an order of magnitude, but the

DOI: 10.1021/acs.jpca.8b00883
J. Phys. Chem. A 2018, 122, 3480−3488

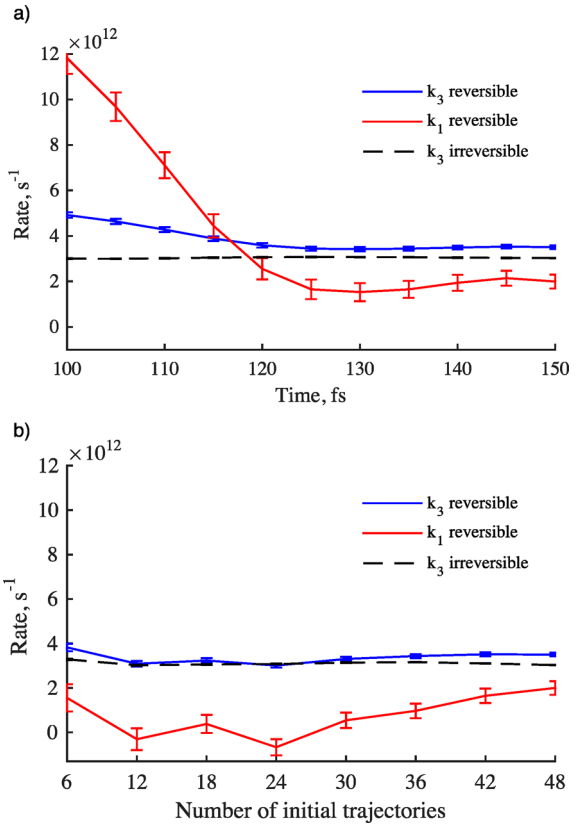

Figure 3. (a) Convergence of the AIMS-DFT rate constants with respect to the simulation time (48 initial trajectories). (b) Convergence of the rate constants with respect to the number of initial trajectories (150 fs simulation time). Blue and red lines represent k_3 and k_1 constants for a reversible reaction (eq 18), respectively. Dashed black line corresponds to the fit for an irreversible reaction. Error bars represent 95% confidence interval.

confidence interval only decreases by a factor of 2. If one is interested in correctly predicting branching ratios that require accurate values for both k_1 and k_3, the convergence analysis must be performed to ensure the sufficient sampling. By contrast, obtaining the rate constant for the irreversible reaction, using the following equation $F_3(t) = \exp\left(-\frac{t}{\tau}\right)$, is significantly easier and requires a smaller number of trajectories and a shorter simulation time. Figure 3b shows that the accurate value of the rate constant, assuming irreversible ISC, can be obtained from as little as six initial trajectories.

This conclusion is not very surprising because, by assuming that the reaction only proceeds in one direction, one effectively defines the asymptotic behavior of the exponent, i.e., population of the excited state goes to zero as time goes to infinity. For larger systems with more degrees of freedom, a larger number of trajectories will be required to achieve a similar convergence of the ISC rate constants. However, predicting the rate of irreversible ISC is still expected to require much smaller number of relatively short trajectories.

The rate constants as functions of internal energy predicted by NA-TST using results of the DFT calculations are presented in Figure 4. Because the LZ formula does not account for quantum tunneling, the probability of transition for internal energies below MECP should be zero. However, because NA-TST accounts for the zero-point energy ($ZPE_{MECP} = (\omega_1 + \omega_2)/2$), the actual threshold below which the LZ rate constants

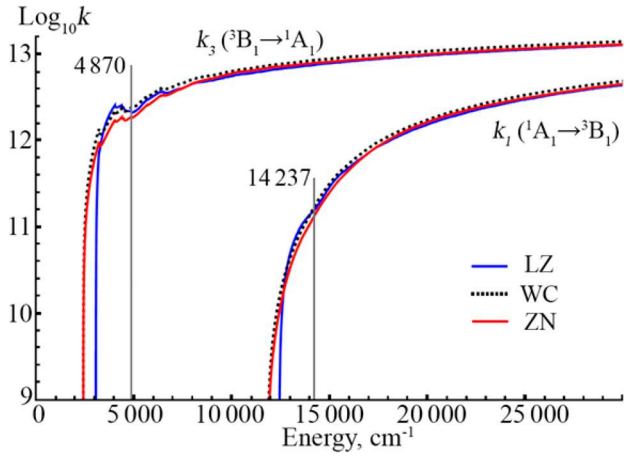

Figure 4. $^3B_1 \rightarrow {}^1A_1$ rate constant k_3 and the $^1A_1 \rightarrow {}^3B_1$ rate constant k_1 as functions of the internal energy obtained with the LZ (blue), WC (dashed black), and ZN (red) transition probability. The plotted rate constants are calculated with NA-TST using the DFT results. The internal energy corresponding to k_3 is relative to the $^3B_1$ minimum; the internal energy corresponding to k_1 is relative to the $^1A_1$ minimum.

are zero is E_{MECP} + ZPE_{MECP}. This corresponds to the thresholds of 12429 cm^{-1} for $^1A_1 \rightarrow {}^3B_1$ transition, and 3062 cm^{-1} for $^3B_1 \rightarrow {}^1A_1$ transition. When transition probability is calculated using the WC and ZN formulas, which account for tunneling, the rate constants are nonzero even for the internal energies below E_{MECP} + ZPE_{MECP}.

The internal energy averaged over all 48 AIMS trajectories is 4870 cm^{-1} with respect to the $^3B_1$ minimum, and 14237 cm^{-1} with respect to the $^1A_1$ minimum. These energies correspond to the NA-TST rate constants of $k_3 = 2.37 \times 10^{12}$ s^{-1}, $k_1 = 1.73 \times 10^{11}$ s^{-1}, and the $^3B_1$ state lifetime τ = 393 fs, for the WC transition probability (Figure 4). The values obtained with the LZ transition probability are $k_3 = 2.16 \times 10^{12}$ s^{-1}, $k_1 = 1.58 \times 10^{11}$ s^{-1}, and τ = 432 fs. The corresponding NA-TST rate constants found with ZN formulas are $k_3 = 1.85 \times 10^{12}$ s^{-1}, $k_1 = 1.35 \times 10^{11}$ s^{-1}, and lifetime τ = 504. The AIMS-CASSCF, AIMS-DFT and NA-TST rate constants and lifetimes are reported in Table 2. The ISC rate constants calculated using the ZN and WC formulas are similar in the tunneling regime, but start to deviate from each other near the MECP. However, all formulas predict transition probabilities approaching each other in the high-energy limit. Keeping in mind the poor accuracy of the LZ formula in the vicinity of MECP and the erroneous behavior of the WC formula for moderate and strong coupling (probability can be larger than unity), the ZN formulas are expected to provide the most reliable transition probabilities for the NA-TST rate calculations.

The NA-TST predicts a longer lifetime than the AIMS dynamics, for both CASSCF and DFT. As was already noted in our previous work,[29] this discrepancy between the AIMS dynamics and NA-TST results can be explained by nonlocal effects: in the NA-TST, a transition between the two states can occur only at the MECP, whereas in the AIMS molecular dynamics, transitions occur anywhere close to the intersection seam where the SOC between electronic states is large. In the present nonoptimized implementation, a 150 fs AIMS-DFT simulation starting from a single trajectory takes about 2 days on a single Intel Xeon X5650 core. By contrast, the similar AIMS-CASSCF simulation takes 8−10 days. The statistical NA-TST calculations with the LZ and WC probabilities take about

DOI: 10.1021/acs.jpca.8b00883
J. Phys. Chem. A 2018, 122, 3480−3488

Table 2. Rate Constants k_3, k_1, and the $^3B_1$ State Lifetime τ Obtained with the AIMS-CASSCF and AIMS-DFT Molecular Dynamics, As Well As with the NA-TST Using the ZN, LZ, and WC Transition Probabilities

	AIMS		NA-TST					
			CASSCF			DFT		
	CASSCF	DFT	ZN	LZ	WC	ZN	LZ	WC
$k_3\times10^{-12}$, s^{-1}	3.78	3.50	2.30	2.89	2.93	1.85	2.16	2.37
$k_1\times10^{-12}$, s^{-1}	1.58	1.99	0.164	0.206	0.209	0.135	0.158	0.173
τ, fs	186	182	406	323	319	504	432	393

a minute, while the calculations using the ZN probabilities require about 10 h.

The AIMS-DFT molecular dynamics method presented in this work can be further improved with the more rigorous approach to calculate the SOC matrix elements. The GAMESS package does not have the capability to calculate SOC with DFT. In principle, DFT-SOC can be implemented within the formalism of the linear response time-dependent density functional theory (LR-TDDFT).[56] The studies of the ISC dynamics using the ground state DFT, as described in this work, are only possible for the lowest-energy states of each spin multiplicity. In the future, we plan to develop an extension based on TDDFT to investigate ISCs between excited electronic states.

V. CONCLUSIONS

We described the implementation of the AIMS method to study the ISC dynamics using the electronic properties obtained with DFT. The population decay from the excited $^3B_1$ to the ground $^1A_1$ state of GeH_2 was used as a test to compare the performance of the AIMS dynamics utilizing different electronic structure methods: CASSCF and DFT. The rate constants for the $^3B_1 \rightarrow {}^1A_1$ and the reverse $^1A_1 \rightarrow {}^3B_1$ ISCs, as well as the lifetime of the $^3B_1$ state were calculated. The ISC rate constants obtained from the AIMS dynamics were compared with the values calculated using the statistical NA-TST approach. In NA-TST, the probability of transitions between the $^3B_1$ and $^1A_1$ states was calculated with the Landau−Zener, weak coupling, and Zhu−Nakamura formulas.

The AIMS-DFT dynamics predicts the $^3B_1 \rightarrow {}^1A_1$ rate constant $k_3 = 3.50 \times 10^{12}$ s^{-1} and the reverse $^1A_1 \rightarrow {}^3B_1$ rate constant $k_1 = 1.99 \times 10^{12}$ s^{-1}. These values are very close to those predicted by AIMS-CASSCF ($k_3 = 3.78 \times 10^{12}$ s^{-1} and $k_1 = 1.58 \times 10^{12}$ s^{-1}). The lifetimes of the $^3B_1$ excited state obtained with the CASSCF-based (186 fs) and DFT-based (182 fs) AIMS dynamics are essentially the same. We believe that this agreement is mostly coincidental and can be explained by the cancellation of two effects influencing the rates. While the higher DFT energy barriers reduce the ISC rates, the stronger DFT spin−orbit coupling increases these rates. Compared to the AIMS-DFT dynamics, the statistical NA-TST predicts a longer (by about factor of 2) lifetime of the $^3B_1$ excited state. The longer $^3B_1$ state lifetime, and the lower ISC rates, predicted by NA-TST are likely related to neglecting the interstate transitions away from the MECP and possibly to the assumption of equal distribution of internal energy among vibrational degrees of freedom. By contrast, in the AIMS molecular dynamics, the interstate transitions can occur at different points around the crossing seam of two PESs.

■ ASSOCIATED CONTENT

Supporting Information

The Supporting Information is available free of charge on the ACS Publications website at DOI: 10.1021/acs.jpca.8b00883.

Population of $^3B_1$ state as a function of time calculated with different values of the spawning threshold Λ_{eff}; details of the Zhu−Nakamura formulas (PDF)

■ AUTHOR INFORMATION

Corresponding Author

*E-mail: svarganov@unr.edu; Phone: +1 (775) 784-1406.

ORCID

Aleksandr O. Lykhin: 0000-0002-9366-5866

Sergey A. Varganov: 0000-0001-8301-3891

Present Address

§Department of Chemistry, Michigan State University, East Lansing, Michigan 48824, United States

Notes

The authors declare no competing financial interest.

■ ACKNOWLEDGMENTS

This work was supported by the National Science Foundation through a CAREER Award (CHE-1654547) to S.A.V. This work used the Extreme Science and Engineering Discovery Environment (XSEDE), which is supported by the National Science Foundation Grant Number ACI-1548562. A.O.L. thanks the RFBR, Government of Krasnoyarsk Territory, and Krasnoyarsk Region Science and Technology Support Fund for Grant No. 16-43-243052.

■ REFERENCES

(1) *Organic Light-Emitting Devices*, 1st ed.; Shinar, J., Ed.; Springer-Verlag: New York, 2004.

(2) Wong, W.-Y.; Wang, X.-Z.; He, Z.; Djurišić, A. B.; Yip, C.-T.; Cheung, K.-Y.; Wang, H.; Mak, C. S. K.; Chan, W.-K. Metallated Conjugated Polymers as a New Avenue Towards High-Efficiency Polymer Solar Cells. *Nat. Mater.* **2007**, *6* (7), 521−527.

(3) Yersin, H.; Rausch, A. F.; Czerwieniec, R.; Hofbeck, T.; Fischer, T. The Triplet State of Organo-Transition Metal Compounds. Triplet Harvesting and Singlet Harvesting for Efficient OLEDs. *Coord. Chem. Rev.* **2011**, *255* (21−22), 2622−2652.

(4) Kaliakin, D. S.; Zaari, R. R.; Varganov, S. A. Effect of H_2 Binding on the Nonadiabatic Transition Probability Between Singlet and Triplet States of the [NiFe]-Hydrogenase Active Site. *J. Phys. Chem. A* **2015**, *119* (6), 1066−1073.

(5) dePolo, G. E.; Kaliakin, D. S.; Varganov, S. A. Spin-Forbidden Transitions Between Electronic States in the Active Site of Rubredoxin. *J. Phys. Chem. A* **2016**, *120* (43), 8691−8698.

(6) Richter, M.; Marquetand, P.; González-Vázquez, J.; Sola, I.; González, L. Femtosecond Intersystem Crossing in the DNA Nucleobase Cytosine. *J. Phys. Chem. Lett.* **2012**, *3* (21), 3090−3095.

(7) Martínez-Fernández, L.; Corral, I.; Granucci, G.; Persico, M. Competing Ultrafast Intersystem Crossing and Internal Conversion: a

DOI: 10.1021/acs.jpca.8b00883
J. Phys. Chem. A 2018, 122, 3480−3488

Time Resolved Picture for the Deactivation of 6-Thioguanine. *Chem. Sci.* **2014**, *5* (4), 1336−12.
(8) Cavaleri, J. J.; Prater, K.; Bowman, R. M. An Investigation of the Solvent Dependence on the Ultrafast Intersystem Crossing Kinetics of Xanthone. *Chem. Phys. Lett.* **1996**, *259*, 495−502.
(9) Satzger, H.; Schmidt, B.; Root, C.; Zinth, W.; et al. Ultrafast Quenching of the Xanthone Triplet by Energy Transfer: New Insight Into the Intersystem Crossing Kinetics. *J. Phys. Chem. A* **2004**, *108*, 10072−10079.
(10) Minns, R. S.; Parker, D. S. N.; Penfold, T. J.; Worth, G. A.; Fielding, H. H. Competing Ultrafast Intersystem Crossing and Internal Conversion in the "Channel 3" Region of Benzene. *Phys. Chem. Chem. Phys.* **2010**, *12* (48), 15607−15615.
(11) Balucani, N.; Leonori, F.; Casavecchia, P.; Fu, B.; Bowman, J. M. Crossed Molecular Beams and Quasiclassical Trajectory Surface Hopping Studies of the Multichannel Nonadiabatic $O(^3P)$ + Ethylene Reaction at High Collision Energy. *J. Phys. Chem. A* **2015**, *119* (50), 12498−12511.
(12) Griesbeck, A. G.; Abe, M.; Bondock, S. Selectivity Control in Electron Spin Inversion Processes: Regio- and Stereochemistry of Paternò−Büchi Photocyclo- Additions as a Powerful Tool for Mapping Intersystem Crossing Processes. *Acc. Chem. Res.* **2004**, *37* (12), 919−928.
(13) McCusker, J. K.; Vlček, A., Jr. Ultrafast Excited-State Processes in Inorganic Systems. *Acc. Chem. Res.* **2015**, *48* (5), 1207−1208.
(14) Auböck, G.; Chergui, M. Sub-50-Fs Photoinduced Spin Crossover in $[Fe(bpy)_3]^{2+}$. *Nat. Chem.* **2015**, *7* (8), 629−633.
(15) Maeda, S.; Taketsugu, T.; Ohno, K.; Morokuma, K. From Roaming Atoms to Hopping Surfaces: Mapping Out Global Reaction Routes in Photochemistry. *J. Am. Chem. Soc.* **2015**, *137* (10), 3433−3445.
(16) Marian, C. M. Spin-Orbit Coupling and Intersystem Crossing in Molecules. *WIREs Comput. Mol. Sci.* **2012**, *2* (2), 187−203.
(17) Zhang, W.; Alonso-Mori, R.; Bergmann, U.; Bressler, C.; et al. Tracking Excited-State Charge and Spin Dynamics in Iron Coordination Complexes. *Nature* **2014**, *509* (7500), 345−348.
(18) Yson, R. L.; Gilgor, J. L.; Guberman, B. A.; Varganov, S. A. Protein Induced Singlet-Triplet Quasidegeneracy in the Active Site of [NiFe]-Hydrogenase. *Chem. Phys. Lett.* **2013**, *577*, 138−141.
(19) Zaari, R. R.; Varganov, S. A. Nonadiabatic Transition State Theory and Trajectory Surface Hopping Dynamics: Intersystem Crossing Between $^3B_1$ and $^1A_1$ States of SiH_2. *J. Phys. Chem. A* **2015**, *119* (8), 1332−1338.
(20) Lorquet, J. C.; Leyh-Nihant, B. Nonadiabatic Unimolecular Reactions. 1. a Statistical Formulation for the Rate Constants. *J. Phys. Chem.* **1988**, *92*, 4778−4783.
(21) Harvey, J. N.; Aschi, M. Spin-Forbidden Dehydrogenation of Methoxy Cation: a Statistical View. *Phys. Chem. Chem. Phys.* **1999**, *1* (24), 5555−5563.
(22) Zener, C. Non-Adiabatic Crossing of Energy Levels. *Proc. R. Soc. London, Ser. A* **1932**, *137* (833), 696−702.
(23) Wittig, C. The Landau-Zener Formula. *J. Phys. Chem. B* **2005**, *109* (17), 8428−8430.
(24) Landau, L. D. *Collected Papers of L. D. Landau*; Ter Haar, D., Ed.; Elsevier, 1965; pp 63−66.
(25) Nikitin, E. E. Nonadiabatic Transition Near the Turning Point in Atomic Collisions. *Opt. Spectrosc.* **1961**, *11*, 246−248.
(26) Delos, J. B. On the Reactions of N_2 with O. *J. Chem. Phys.* **1973**, *59* (5), 2365−2369.
(27) Nakamura, H. *Nonadiabatic Transition: Concepts, Basic Theories and Applications*, 2nd ed.; World Scientific Publishing Co. Pte. Ltd.: Singapore, 2012.
(28) Ben-Nun, M.; Martinez, T. J. Ab Initio Quantum Molecular Dynamics. *Adv. Chem. Phys.* **2002**, *121*, 439−512.
(29) Fedorov, D. A.; Pruitt, S. R.; Keipert, K.; Gordon, M. S.; Varganov, S. A. Ab Initio Multiple Spawning Method for Intersystem Crossing Dynamics: Spin-Forbidden Transitions Between $^3B_1$ and $^1A_1$ States of GeH_2. *J. Phys. Chem. A* **2016**, *120* (18), 2911−2919.
(30) Curchod, B. F. E.; Rauer, C.; Marquetand, P.; González, L.; Martínez, T. J. Communication: GAIMS—Generalized Ab Initio Multiple Spawning for Both Internal Conversion and Intersystem Crossing Processes. *J. Chem. Phys.* **2016**, *144* (10), 101102−101107.
(31) Lykhin, A. O.; Kaliakin, D. S.; dePolo, G. E.; Kuzubov, A. A.; Varganov, S. A. Nonadiabatic Transition State Theory: Application to Intersystem Crossings in the Active Sites of Metal-Sulfur Proteins. *Int. J. Quantum Chem.* **2016**, *116*, 750.
(32) Jasper, A. W. Multidimensional Effects in Nonadiabatic Statistical Theories of Spin-Forbidden Kinetics: a Case Study of $^3O + CO \rightarrow CO_2$. *J. Phys. Chem. A* **2015**, *119* (28), 7339−7351.
(33) Harvey, J. N. Understanding the Kinetics of Spin-Forbidden Chemical Reactions. *Phys. Chem. Chem. Phys.* **2007**, *9* (3), 331.
(34) Nikitin, E. E.; Umanskii, S. Y. *Theory of Slow Atomic Collisions*; Springer-Verlag: Berlin Heidelberg, New York, 1984.
(35) Zhu, C.; Nakamura, H. The Two-State Linear Curve Crossing Problems Revisited. II. Analytical Approximations for the Stokes Constant and Scattering Matrix: the Landau−Zener Case. *J. Chem. Phys.* **1992**, *97* (11), 8497−8514.
(36) Zhu, C. Y.; Teranishi, Y.; Nakamura, H. Nonadiabatic Transitions Due to Curve Crossings: Complete Solutions of the Landau-Zener-Stueckelberg Problems and Their Applications. *Adv. Chem. Phys.* **2007**, *117*, 127−233.
(37) Ishida, T.; Nanbu, S.; Nakamura, H. Clarification of Non-adiabatic Chemical Dynamics by the Zhu-Nakamura Theory of Nonadiabatic Transition: From Tri-Atomic Systems to Reactions in Solutions. *Int. Rev. Phys. Chem.* **2017**, *36*, 229.
(38) Baer, T.; Hase, W. L. *Unimolecular Reaction Dynamics: Theory and Experiments*; Oxford University Press: New York, 1995.
(39) Green, N. J. B. *Unimolecular Kinetics, Part 1. the Reaction Step*; Green, N. J. B., Ed.; Elsevier Science: Amsterdam, 2003.
(40) Ben-Nun, M.; Martínez, T. J. Nonadiabatic Molecular Dynamics: Validation of the Multiple Spawning Method for a Multidimensional Problem. *J. Chem. Phys.* **1998**, *108* (17), 7244.
(41) Ben-Nun, M.; Quenneville, J.; Martínez, T. J. Ab Initio Multiple Spawning: Photochemistry From First Principles Quantum Molecular Dynamics. *J. Phys. Chem. A* **2000**, *104* (22), 5161−5175.
(42) Martinez, T. J.; Ben-Nun, M.; Levine, R. D. Multi-Electronic-State Molecular Dynamics: a Wave Function Approach with Applications. *J. Phys. Chem.* **1996**, *100*, 7884−7895.
(43) Thompson, A. L.; Punwong, C.; Martínez, T. J. Optimization of Width Parameters for Quantum Dynamics with Frozen Gaussian Basis Sets. *Chem. Phys.* **2010**, *370* (1−3), 70−77.
(44) Mathews, J.; Walker, R. L. *Mathematical Methods of Physics*; W. A. Benjamin: New York, 1980.
(45) Granucci, G.; Persico, M.; Spighi, G. Surface Hopping Trajectory Simulations with Spin-Orbit and Dynamical Couplings. *J. Chem. Phys.* **2012**, *137* (22), 22A501.
(46) Bethe, H. A.; Salpeter, E. E. *Quantum Mechanics of the One and Two Electron Atoms*; Plenum: New York, 1977.
(47) Martinez, T. J.; Ben-Nun, M.; Levine, R. D. Molecular Collision Dynamics on Several Electronic States. *J. Phys. Chem. A* **1997**, *101*, 6389−6402.
(48) Granucci, G.; Persico, M. Critical Appraisal of the Fewest Switches Algorithm for Surface Hopping. *J. Chem. Phys.* **2007**, *126* (13), 134114.
(49) Roos, B. O. *Advances in Chemical Physics*; Wiley Interscience: New York, 1987; Vol. *69*, pp 339−445.
(50) Becke, A. D. Density Functional Calculations of Molecular Bond Energies. *J. Chem. Phys.* **1986**, *84* (8), 4524−4529.
(51) Lee, C.; Yang, W.; Parr, R. G. Development of the Colle-Salvetti Correlation-Energy Formula Into a Functional of the Electron Density. *Phys. Rev. B: Condens. Matter Mater. Phys.* **1988**, *37* (2), 785−789.
(52) Becke, A. Density-Functional Exchange-Energy Approximation with Correct Asymptotic Behavior. *Phys. Rev. A: At., Mol., Opt. Phys.* **1988**, *38* (6), 3098−3100.
(53) Fedorov, D. G.; Gordon, M. S. A Study of the Relative Importance of One and Two-Electron Contributions to Spin−Orbit Coupling. *J. Chem. Phys.* **2000**, *112* (13), 5611.

DOI: 10.1021/acs.jpca.8b00883
J. Phys. Chem. A 2018, 122, 3480−3488

(54) Hillery, M.; O'connell, R. F.; Scully, M. O.; Wigner, E. P. Distribution Functions in Physics: Fundamentals. *Phys. Rep.* **1984**, *106*, 121−167.
(55) Gaenko, A.; DeFusco, A.; Varganov, S. A.; Martínez, T. J.; Gordon, M. S. Interfacing the Ab Initio Multiple Spawning Method with Electronic Structure Methods in GAMESS: Photodecay of Trans-Azomethane. *J. Phys. Chem. A* **2014**, *118* (46), 10902−10908.
(56) Franco de Carvalho, F.; Curchod, B. F. E.; Penfold, T. J.; Tavernelli, I. Derivation of Spin-Orbit Couplings in Collinear Linear-Response TDDFT: a Rigorous Formulation. *J. Chem. Phys.* **2014**, *140* (14), 144103−144113.

DOI: 10.1021/acs.jpca.8b00883
J. Phys. Chem. A 2018, 122, 3480−3488